Symmetry Breaking and the Twisted Elastic Ring

Robert S. Manning and John H. Maddocks*

Département de Mathématiques
École Polytechnique Fédérale de Lausanne
CH-1015 Lausanne SWITZERLAND

http://lcvmwww.epfl.ch/
rmanning@masg1.epfl.ch, maddocks@dma.epfl.ch

May 19, 1998

Abstract

Symmetry breaking is considered in the context of a parameter-dependent two-point boundary value problem describing a twisted elastic ring that arises as a model of DNA minicircles. We explicitly determine, via a perturbation expansion, those representatives of a manifold of solutions to a symmetric BVP that persist when the symmetry is broken. Conditions generating a generic splitting are identified, and some degenerate cases are studied. In both the generic and degenerate cases, the results of the perturbation expansion are used to improve the efficiency of existing algorithms for computing symmetry-broken bifurcation diagrams.

*Author to whom correspondence should be addressed.

1 Introduction

The presence of one or more continuous symmetries in parameter-dependent nonlinear two-point boundary value problems (BVPs) poses unique challenges. On the one hand, symmetry often leads to well-structured bifurcation diagrams, along with the ability to push analytic techniques further than would be typically possible. As such, a symmetric case of a BVP is often a fruitful starting point in the study of the general case. On the other hand, from a computational point of view, the presence of symmetry, with a corresponding need for symmetry-breaking from the symmetric to asymmetric case, generally requires a careful re-examination of traditional numerical techniques. In particular, for parameter continuation algorithms, singularity of the linearized operator caused by symmetry-generated families of equilibria can cause difficulties.

Here we focus on the above phenomenon in the particular example of the twisted ring, in which an elastic rod is closed into a loop with an imposed twist angle α. The relevant symmetric BVP (which we call the *perfect problem*) pertains to the case of an intrinsically straight, uniform rod with equal bending stiffnesses. Symmetry-breaking arises when intrinsic curvature is added to the rod (via a homotopy parameter ϵ), e.g. to model DNA intrinsic curvature due to base-pair interactions or protein-binding (see, e.g. [2, 3, 11, 14]).

The starting point for our analysis will be the article of Li and Maddocks [10], which describes both the perfect problem and a rudimentary technique for symmetry-breaking. The symmetries of the perfect problem imply that for each value of α, the BVP representing the twisted ring has a continuous, symmetry-related family of solutions (isomorphic to either a circle or a torus), which we will call here the *orbit* (following the terminology in algebra for the set of images of a group action). Since the solutions in this orbit are interrelated by simple symmetry operations, it is numerically most efficient to compute only a single representative of the orbit. In fact, a significant portion of [10] is devoted to devising an adapted BVP for computing isolated representatives of solutions from this orbit, but the particular details of these computations on the perfect problem will not be a major concern here. Rather, we are concerned with using the perfect solution set as an organizing center for more general *imperfect problems* via symmetry-breaking techniques.

When symmetry is broken, the entire orbit will not in general persist, but will instead degenerate into several isolated solutions of the perturbed problem. We will denote the representatives of the orbit that persist in the perturbed problem as *ϵ-bifurcation points*, because they are locations where, at fixed α, a branch of imperfect solutions ($\epsilon > 0$) intersects the orbit of perfect solutions ($\epsilon = 0$). (We will also have occasion to discuss *α-bifurcation points*, i.e. intersections of solution branches for fixed ϵ and varying α). The computational challenge in symmetry-breaking is that the locations of the ϵ-bifurcation points on the orbit depend on the nature of the symmetry-breaking perturbation, and may be quite far from any particular starting point chosen on the orbit. In [10], this computational challenge is met by using a parameter-continuation algorithm, in which the orbit is traversed numerically, and bifurcating solutions to the asymmetric case (generally two if the orbit is a circle or four if it is a torus) are recorded as singularities in an appropriate Jacobian. Unfortunately, this approach has several limitations, which we propose to address in this paper. First, significant computation is devoted to numerically determining solutions on the orbit exclusively for the purpose of finding the ϵ-bifurcation points. This computational procedure is particularly delicate when the orbit has dimension greater than one (e.g. the case in which the orbit is a torus), since the parameter-continuation algorithm used (pseudo-arclength as implemented in AUTO [5]) is inherently one-dimensional. Second, the approach gives no forewarning of particular degenerate types of symmetry-breaking which can lead to unusual structures in the imperfect bifurcation diagram, e.g. more than the generically expected number of bifurcating branches. Identifying such degenerate cases is of considerable interest (see for example the analysis in Sec. 9 of a phenomenon observed numerically in [8]).

In this paper, we present a perturbation expansion for locating the ϵ-bifurcation points on the orbit in an explicit fashion. The general perturbation procedure is comparatively standard in that it uses solvability conditions at various orders of the expansion (see, e.g. [1, p. 166]), although the setting here is somewhat unusual (e.g., the central differential operator considered here depends on ϵ, and bifurcation occurs from a manifold of solutions). Our perturbation expansion enables the design of an improved symmetry-breaking algorithm in which the appropriate starting point on the orbit can be identified so that a direct transfer to the bifurcating branch is possible. At the same time, the perturbation calculation allows the analysis of particular perturbations to the symmetric problem that lead to unusual, "non-generic", behaviors, which serves both as a warning in computations, and as a potential guide in designing imperfect problems with certain desired properties (e.g. multiple stable solutions).

2 The Twisted Elastic Ring

We begin by summarizing the formulation presented in [4, 10] of the special Cosserat theory (see, e.g. [1]), commonly used in continuum mechanics to model an inextensible and unshearable rod, or an *elastica*. For each value of arclength s along the rod ($0 \leq s \leq 1$), the centerline is denoted by $\mathbf{r}(s)$, and the orientation of the rod cross-section is given by an orthonormal frame of directors $(\mathbf{d}_1(s), \mathbf{d}_2(s), \mathbf{d}_3(s))$. Under the assumption of inextensibility and unshearability, the cross-section normal vector $\mathbf{d}_3$ coincides with the unit tangent vector to the centerline $\mathbf{r}'$ (differentiation by s being denoted throughout by a prime). This restriction leaves one degree of freedom in the orthonormal frame: the orientation of $(\mathbf{d}_1, \mathbf{d}_2)$ in the plane of the cross-section. We may thus visualize an elastica as in Fig. 1, with the $\mathbf{r}(s)$ represented as a tube and $\mathbf{d}_1(s)$ as a ribbon.

The *strains* $\mathsf{u}(s) = (u_1(s), u_2(s), u_3(s))$ of any rod configuration are given by the expressions

$$u_i \equiv \mathbf{u}^T \mathbf{d}_i, \quad i = 1, 2, 3,$$

where the Darboux vector $\mathbf{u}$ is defined by

$$\mathbf{d}_i' = \mathbf{u} \times \mathbf{d}_i, \quad i = 1, 2, 3. \tag{1}$$

In the absence of external forces, we assume the rod has a unique minimal-energy shape, or *intrinsic shape*. The strains corresponding to the intrinsic shape are denoted by $\hat{\mathsf{u}}(s)$.

Under the assumption of hyperelasticity, the strains u_i determine local moments m_i acting on the rod cross-section by the relation

$$m_i = \frac{\partial W}{\partial u_i},$$

for a material-dependent strain-energy density function $W(\mathsf{u} - \hat{\mathsf{u}}, s)$. In this paper, we further assume the particular form

$$W(\mathsf{u} - \hat{\mathsf{u}}, s) = \sum_{i=1}^{3} K_i (u_i - \hat{u}_i)^2, \quad K_1 = K_2, \tag{2}$$

which is strictly convex in $\mathsf{u} - \hat{\mathsf{u}}$ and has a minimum at $\mathsf{u} - \hat{\mathsf{u}} = (0, 0, 0)$, although the procedures we describe could similarly be applied to other strain-energy functions. Further, in all computed examples, we take $K_3 = 1.5K_1$, although the theoretical results presented hold for arbitrary values of K_3 and the computations could readily be repeated for any other value.

With the above assumptions and notation, the equilibrium configurations of a rod are critical, or stationary, points of the energy $\int_0^1 W ds$ subject to appropriate boundary conditions. As shown in [4, 10], the corresponding system of second-order Euler-Lagrange ordinary differential equations (ODEs) for the equilibrium configurations of a rod can be rewritten as an equivalent Hamiltonian system of first-order ODEs with Hamiltonian

$$H = \sum_{i=1}^{3} \left[\frac{(\boldsymbol{\mu}^T \mathbf{B}_i \mathbf{q})^2}{8K_i} + \frac{\hat{u}_i (\boldsymbol{\mu}^T \mathbf{B}_i \mathbf{q})}{2} \right] + \mathbf{n}^T \mathbf{d}_3(\mathbf{q}),$$

and "evolution" in arclength s. Written out explicitly, the ODEs governing equilibrium are:

$$\begin{aligned}
\mathbf{r}' &= \frac{\partial H}{\partial \mathbf{n}} = \mathbf{d}_3(\mathbf{q}), \\
\mathbf{q}' &= \frac{\partial H}{\partial \boldsymbol{\mu}} = \frac{1}{2} \sum_{i=1}^{3} u_i(\boldsymbol{\mu}, \mathbf{q}) \mathbf{B}_i \mathbf{q}, \\
\mathbf{n}' &= -\frac{\partial H}{\partial \mathbf{r}} = \mathbf{0}, \\
\boldsymbol{\mu}' &= -\frac{\partial H}{\partial \mathbf{q}} = \frac{1}{2} \sum_{i=1}^{3} u_i(\boldsymbol{\mu}, \mathbf{q}) \mathbf{B}_i \boldsymbol{\mu} - \frac{\partial \mathbf{d}_3}{\partial \mathbf{q}}^T \mathbf{n},
\end{aligned} \tag{3}$$

where

$$\mathbf{d}_3(\mathbf{q}) = \begin{bmatrix} 2q_1q_3 + 2q_2q_4 \\ 2q_2q_3 - 2q_1q_4 \\ -q_1^2 - q_2^2 + q_3^2 + q_4^2 \end{bmatrix}, \quad \frac{\partial \mathbf{d}_3}{\partial \mathbf{q}} = 2 \begin{bmatrix} q_3 & q_4 & q_1 & q_2 \\ -q_4 & q_3 & q_2 & -q_1 \\ -q_1 & -q_2 & q_3 & q_4 \end{bmatrix},$$

$$u_i(\boldsymbol{\mu}, \mathbf{q}) = \epsilon \hat{u}_i + \frac{\boldsymbol{\mu}^T \mathbf{B}_i \mathbf{q}}{2K_i}, \tag{4}$$

(the parameter ϵ is included for convenience of use in Sec. 4), and

$$\mathbf{B}_1 = \begin{bmatrix} 0 & 0 & 0 & 1 \\ 0 & 0 & 1 & 0 \\ 0 & -1 & 0 & 0 \\ -1 & 0 & 0 & 0 \end{bmatrix}, \ \mathbf{B}_2 = \begin{bmatrix} 0 & 0 & -1 & 0 \\ 0 & 0 & 0 & 1 \\ 1 & 0 & 0 & 0 \\ 0 & -1 & 0 & 0 \end{bmatrix}, \ \mathbf{B}_3 = \begin{bmatrix} 0 & 1 & 0 & 0 \\ -1 & 0 & 0 & 0 \\ 0 & 0 & 0 & 1 \\ 0 & 0 & -1 & 0 \end{bmatrix}.$$

Here, $\mathbf{q} \in \mathbb{R}^4$ are *Euler parameters* (or *quaternions*) used to parameterize the directors $(\mathbf{d}_1, \mathbf{d}_2, \mathbf{d}_3) \in SO(3)$:

$$\begin{aligned} \mathbf{R}(\mathbf{q}) &\equiv \begin{bmatrix} \mathbf{d}_1(\mathbf{q}) & \mathbf{d}_2(\mathbf{q}) & \mathbf{d}_3(\mathbf{q}) \end{bmatrix} \\ &= \begin{bmatrix} q_1^2 - q_2^2 - q_3^2 + q_4^2 & 2q_1q_2 - 2q_3q_4 & 2q_1q_3 + 2q_2q_4 \\ 2q_1q_2 + 2q_3q_4 & -q_1^2 + q_2^2 - q_3^2 + q_4^2 & 2q_2q_3 - 2q_1q_4 \\ 2q_1q_3 - 2q_2q_4 & 2q_2q_3 + 2q_1q_4 & -q_1^2 - q_2^2 + q_3^2 + q_4^2 \end{bmatrix}. \end{aligned} \tag{5}$$

The variable $\mathbf{n} \in \mathbb{R}^3$ is conjugate to the centerline $\mathbf{r}$ and represents the force (or integrated stress) of the interval on one side of the cross section on the interval on the other. The variable $\boldsymbol{\mu} \in \mathbb{R}^4$ is conjugate to $\mathbf{q}$:

$$\boldsymbol{\mu} \equiv -2(\mathbf{n}^T\mathbf{r})\mathbf{q} + 4\sum_{i=1}^{3} K_i \left[(\mathbf{q}')^T\mathbf{B}_i\mathbf{q}\right] \mathbf{B}_i\mathbf{q}. \tag{6}$$

The ODEs (3) must be augmented with appropriate boundary conditions. In this article, we consider the twisted elastic ring shown in Fig. 2, which corresponds to the boundary conditions:

$$\begin{aligned} \mathbf{r}(0) &= \langle 0,0,0\rangle, \ \ \mathbf{r}(1) = \langle 0,0,0\rangle, \ \ q_1(0) = q_2(0) = q_3(0) = 0, \\ \mathbf{q}(1) &= \langle 0, 0, -\sin(\alpha/2), -\cos(\alpha/2)\rangle, \ \ \mu_4(0) = 0. \end{aligned} \tag{7}$$

The boundary conditions on $\mathbf{r}$ and $\mathbf{q}$ at $s = 0$ are needed to eliminate translational and rotational rigid body freedoms by aligning the $s = 0$ director frame with the fixed xyz frame. As discussed in [10], the non-intuitive condition $\mu_4(0) = 0$ removes a gauge freedom that is an artifact of the use of $\mathbf{q} \in \mathbb{R}^4$ to parameterize the locally 3-dimensional group $(\mathbf{d}_1, \mathbf{d}_2, \mathbf{d}_3) \in SO(3)$. Throughout this article, a *ring equilibrium* denotes a solution $(\mathbf{r}, \mathbf{q}, \mathbf{n}, \boldsymbol{\mu})$ to the differential equations (3) subject to boundary conditions (7).

The principal goal of this article is to understand the set of ring equilibria in the transition from the symmetric *perfect problem* $\hat{u}_i(s) \equiv 0$ to other *imperfect problems* with small but nonzero $\hat{u}_i(s)$. The perfect problem has been the subject of study by many authors, but we defer to [9, 10] for a discussion of the literature. Here we follow the notation and formulation that are described in detail in [4, 10].

The set of ring equilibria for the perfect problem as the parameter α is varied is shown in Fig. 3. This *perfect diagram* is described in detail in [10]. The parabolic (or *trivial*) branches in the perfect diagram represent configurations with N-fold-covered circular centerlines and constant twist rates, and the solutions on these branches can be written in closed form:

$$\begin{aligned}
\mathbf{r}_0(s) &= \frac{1}{2N\pi}\begin{bmatrix} 0 \\ \cos(2N\pi s)-1 \\ \sin(2N\pi s)\end{bmatrix}, \quad \mathbf{q}_0(s) = \begin{bmatrix} \cos(\alpha s/2)\sin(N\pi s) \\ -\sin(\alpha s/2)\sin(N\pi s) \\ \sin(\alpha s/2)\cos(N\pi s) \\ \cos(\alpha s/2)\cos(N\pi s)\end{bmatrix} \\
\mathbf{n}_0(s) &= \begin{bmatrix} 2K_3N\alpha\pi \\ 0 \\ 0 \end{bmatrix}, \\
\boldsymbol{\mu}_0(s) &= \begin{bmatrix} 4K_1N\pi\cos(\alpha s/2)\cos(N\pi s) - 2K_3\alpha\sin(\alpha s/2)\sin(N\pi s) \\ -4K_1N\pi\sin(\alpha s/2)\cos(N\pi s) - 2K_3\alpha\cos(\alpha s/2)\sin(N\pi s) \\ -4K_1N\pi\sin(\alpha s/2)\sin(N\pi s) + 2K_3\alpha\cos(\alpha s/2)\cos(N\pi s) \\ -4K_1N\pi\cos(\alpha s/2)\sin(N\pi s) - 2K_3\alpha\sin(\alpha s/2)\cos(N\pi s) \end{bmatrix}.
\end{aligned} \tag{8}$$

The trivial branches on the left side of the diagram have $\alpha < 0$, while those on the right have $\alpha > 0$. Each trivial branch contains a countable set of α-bifurcation points, which we label by $M = 1, 2, 3, \ldots$, and for convenience we will denote the vertex of the trivial branch as a 0th bifurcation point. The portion of the N-covered-circle trivial branch between bifurcation points $M-1$ and M will be called the $(N, M, \pm)$ *trivial segment*, or $(N, M, \pm)^{triv}$, where the third argument indicates the sign of α .

The remaining branches in Fig. 3 are denoted as *nontrivial* and contain equilibria with non-planar centerlines, except for a few exceptional configurations such as the figure-eight (cf. [6]). We label a nontrivial branch as $(N, M, \pm)^{nontriv}$ if it begins at the $(N, M, \pm)$ bifurcation point (i.e. the top of $(N, M, \pm)^{triv}$); because of the connectivity of the perfect diagram described in [10], $(N, M, +)^{nontriv}$ and $(M, N, -)^{nontriv}$ denote the same branch.

3 Consequences of symmetry on the set of ring equilibria

A significant portion of the analysis in [10] is devoted to understanding the implications of the (continuous variational) symmetries of uniformity and transverse isotropy on the computation of ring equilibria. Here we make the action of these symmetries explicit. In particular, given any ring equilibrium $\mathbf{z}_0 \equiv (\mathbf{r}_0, \mathbf{q}_0, \mathbf{n}_0, \boldsymbol{\mu}_0)$ for the perfect problem, an orbit of other perfect ring equilibria (for the same α) $\mathbf{z}_{\theta\beta} \equiv (\mathbf{r}_{\theta\beta}, \mathbf{q}_{\theta\beta}, \mathbf{n}_{\theta\beta}, \boldsymbol{\mu}_{\theta\beta})$ may be generated by the application of the following transformations (see Figs. 4 and 5).

Transformation I (associated with the symmetry of transverse isotropy): For $0 \le \theta < 2\pi$,
Step 1: Rotate the ring rigidly by an angle θ about the z axis.[†]
Step 2: Locally rotate the rod about its tangent vector $\mathbf{r}'$ by an angle $-\theta$.

Transformation II (associated with the symmetry of uniformity): For $0 \le \beta < 1$,
Step 1: Translate the rod by $-\mathbf{r}_0(\beta)$ and reparameterize so that $s = 0$ is at the origin.

[†]Here and throughout, an angle of rotation is described as positive or negative as the direction of rotation follows the right-handed or left-handed rule respectively.

Step 2: For each $s > 1-\beta$, locally rotate the rod about its tangent vector $\mathbf{r}'$ by α (to make the ribbon discontinuity occur at $s=0$ instead of $s = 1-\beta$).

Step 3: Rotate the ring rigidly by $\mathbf{R}(\mathbf{q}_0(\beta))^T$ (to satisfy the boundary conditions on $\mathbf{d}_i(0)$).

Note that these transformations generate solutions of the entire BVP and not only of the ODEs. In particular, each transformation couples a material symmetry (transverse isotropy or uniformity) with rigid body symmetries (rotation and translation) to ensure that both the differential equations and boundary conditions are satisfied.

The two transformations can also be written algebraically:

$$\begin{aligned}
\mathbf{r}_{\theta\beta}(s) &= \mathbf{M}_3(\theta)\mathbf{R}(\mathbf{q}_0(\beta))^T\left[\mathbf{r}_0\Big((s+\beta)(\mathrm{mod}\ 1)\Big) - \mathbf{r}_0(\beta)\right], \\
\mathbf{q}_{\theta\beta}(s) &= \mathbf{M}_4(\theta, s+\beta)\left[\mathbf{q}_0(\beta)^T \odot \mathbf{q}_0\Big((s+\beta)(\mathrm{mod}\ 1)\Big)\right], \\
\mathbf{n}_{\theta\beta}(s) &= \mathbf{M}_3(\theta)\mathbf{R}(\mathbf{q}_0(\beta))^T\mathbf{n}_0\Big((s+\beta)(\mathrm{mod}\ 1)\Big), \\
\boldsymbol{\mu}_{\theta\beta}(s) &= \mathbf{M}_4(\theta, s+\beta)\left[\mathbf{q}_0(\beta)^T \odot \boldsymbol{\mu}_0\Big((s+\beta)(\mathrm{mod}\ 1)\Big)\right],
\end{aligned} \tag{9}$$

where the matrices $\mathbf{M}_3$ and $\mathbf{M}_4$ are defined as:

$$\mathbf{M}_3(\theta) \equiv \begin{bmatrix} \cos\theta & \sin\theta & 0 \\ -\sin\theta & \cos\theta & 0 \\ 0 & 0 & 1 \end{bmatrix},$$

$$\mathbf{M}_4(\theta, t) \equiv \begin{cases} \begin{bmatrix} \cos\theta & \sin\theta & 0 & 0 \\ -\sin\theta & \cos\theta & 0 & 0 \\ 0 & 0 & 1 & 0 \\ 0 & 0 & 0 & 1 \end{bmatrix} & \text{if } t < 1 \\ \begin{bmatrix} -\cos(\theta+\frac{\alpha}{2}) & -\sin(\theta+\frac{\alpha}{2}) & 0 & 0 \\ \sin(\theta+\frac{\alpha}{2}) & -\cos(\theta+\frac{\alpha}{2}) & 0 & 0 \\ 0 & 0 & -\cos(\frac{\alpha}{2}) & -\sin(\frac{\alpha}{2}) \\ 0 & 0 & \sin(\frac{\alpha}{2}) & -\cos(\frac{\alpha}{2}) \end{bmatrix} & \text{if } t \geq 1. \end{cases}$$

Here the transpose of a quaternion is defined as:

$$\begin{bmatrix} q_1 \\ q_2 \\ q_3 \\ q_4 \end{bmatrix}^T \equiv \begin{bmatrix} -q_1 \\ -q_2 \\ -q_3 \\ q_4 \end{bmatrix},$$

and the operation $\odot$ represents *quaternion multiplication* defined by (see, e.g. [7], Ch. 21.1, but with the fourth quaternion written first):

$$\begin{bmatrix} q_1 \\ q_2 \\ q_3 \\ q_4 \end{bmatrix} \odot \begin{bmatrix} p_1 \\ p_2 \\ p_3 \\ p_4 \end{bmatrix} = \begin{bmatrix} q_4p_1 - q_3p_2 + q_2p_3 + q_1p_4 \\ q_3p_1 + q_4p_2 - q_1p_3 + q_2p_4 \\ -q_2p_1 + q_1p_2 + q_4p_3 + q_3p_4 \\ -q_1p_1 - q_2p_2 - q_3p_3 + q_4p_4 \end{bmatrix}.$$

Since $\mathbf{r}$ and $\mathbf{n}$ represent physical 3-vectors in the twisted ring problem, the formulae in (9) for $\mathbf{r}_{\theta\beta}$ and $\mathbf{n}_{\theta\beta}$ follow fairly immediately from the descriptions the symmetries. Each director $\mathbf{d}_i$ transforms in the same way as $\mathbf{n}$, from which the formula for $\mathbf{q}_{\theta\beta}$ follows using (5); matrix multiplication of $\mathbf{R}(\mathbf{q})$ becomes quaternion multiplication of the $\mathbf{q}$. Finally, the formula for $\boldsymbol{\mu}_{\theta\beta}$ follows from inserting $(\mathbf{r}_{\theta\beta}, \mathbf{q}_{\theta\beta}, \mathbf{n}_{\theta\beta})$ into the definition (6) of $\boldsymbol{\mu}$, followed by significant simplification.

It is easily verified that these symmetries commute (i.e., we arrive at the same image $\mathbf{z}_{\theta\beta}$ whether we apply Transformation I and then Transformation II, or vice versa). It is also clear that

$$\lim_{\theta\to 2\pi} \mathbf{z}_{\theta\beta} = \mathbf{z}_{0\beta}.$$

If $\mathbf{z}_0$ is on a trivial branch, then, using the closed-form expressions (8), we may verify that $\mathbf{z}_{\theta\beta} = \mathbf{z}_{\bar{\theta}0}$ for $\bar{\theta} = \theta + \alpha\beta \pmod{2\pi}$, effectively removing the β dependence of the orbit (essentially because the circular centerline is invariant under arclength shift). On the other hand, $\mathbf{z}_{\theta_1 0} = \mathbf{z}_{\theta_2 0}$ if and only if $\theta_1 = \theta_2$. Thus, the orbit $\mathcal{S}(\mathbf{z}_0)$ of a ring equilibrium $\mathbf{z}_0$ on a trivial branch of Fig. 3 is isomorphic to a *circle* generated by transverse isotropy:

$$\mathcal{S}_{triv}(\mathbf{z}_0) = \{\mathbf{z}_{\theta 0} : 0 \le \theta < 2\pi\} \sim S^1.$$

If $\mathbf{z}_0$ is on an (M, N) nontrivial branch, numerics indicate that there exists an angle $\Delta\theta$ such that

$$\mathbf{z}_{\theta_1\beta_1} = \mathbf{z}_{\theta_2\beta_2} \Longleftrightarrow (M+N)(\beta_2 - \beta_1) \in \mathbb{Z}, \quad \theta_2 = \theta_1 + \Delta\theta \pmod{2\pi}. \tag{10}$$

Thus, the orbit corresponding to a ring equilibrium on an (M, N) nontrivial branch is isomorphic to a *torus*:

$$\mathcal{S}_{nontriv}(\mathbf{z}_0) = \{\mathbf{z}_{\theta\beta} : 0 \le \theta < 2\pi, \ \ 0 \le \beta < \frac{1}{M+N}\} \sim T^2.$$

(The fact that $\mathbf{z}_0$ is a ring leads fairly immediately to the topology of the orbit being a torus with $0 \le \theta < 2\pi$ and $0 \le \beta < 1$; here we make the stronger observation that in fact the orbit is completely covered by a smaller range of β values $0 \le \beta < 1/(M+N)$, due to a discrete symmetry of $\mathbf{z}_0$ on $(M, N, \pm)^{nontriv}$). There are at least two possible approaches to proving (10). The ODEs (3) are explicitly integrable when $\epsilon = 0$, from which the periodicity of a solution to any *initial* value problem involving these ODEs may be obtained from either a phase plane analysis or using explicit expressions in terms of elliptic functions (see, e.g. [6, 9] for discussions of this issue and citations to the literature). However, we know of no detailed proof that the *particular* period $\frac{1}{M+N}$ is active on the branch $(N, M, \pm)^{nontriv}$ of the BVP (3,7), and we instead rely on the numerics.

In summary, each point on a trivial branch in Fig. 3 represents an entire circle $\mathcal{S}_{triv}(\mathbf{z}_0)$ of ring equilibria (all with the same values of E and m_3), while each point on a nontrivial branch represents a torus $\mathcal{S}_{nontriv}(\mathbf{z}_0)$ of ring equilibria (again all with the same E and m_3).

4 Computing perfect and imperfect ring equilibria

Since we have the explicit formula (9) relating a perfect ring equilibrium $\mathbf{z}_0$ to its orbit $\mathcal{S}(\mathbf{z}_0)$, it suffices in computing the perfect diagram to determine a single representative of the orbit. When seeking to compute ring equilibria for an imperfect problem, a natural approach is to use parameter continuation (such as with the package AUTO [5]), choosing the imperfection parameter ϵ for the continuation parameter (cf. (4)), with an initial value $\epsilon = 0$, and taking as an initial solution $\mathbf{z}$ some particular representative of the orbit of a perfect ring equilibrium as described above. When the continuation parameter ϵ reaches 1, we will have determined a valid imperfect ring equilibrium, at which point we may switch to continuation in another parameter of interest, such as α.

The challenge, as described in Sec. 1, is that the orbit of perfect ring equilibria (corresponding to $\epsilon = 0$) perturbs in general to only a finite set of $\epsilon > 0$ branches of imperfect ring equilibria, and the ϵ-bifurcation points where these imperfect branches bifurcate from the orbit may be quite far from the chosen orbit representative. Li and Maddocks [10] proposed one algorithm for locating these ϵ-bifurcation points numerically. In the case of a circular orbit $\mathcal{S}_{triv}(\mathbf{z}_0)$, a sufficiently robust parameter continuation algorithm (such as AUTO) can locate the bifurcating branches automatically: if we choose ϵ as the continuation parameter with initial value $\epsilon = 0$ and choose as an initial solution any representative of the perfect orbit $\mathbf{z}_{\theta_0 0}$, the code will automatically follow the orbit $\mathcal{S}_{triv}(\mathbf{z}_0)$ leaving $\epsilon = 0$ fixed (thus tracking a highly degenerate fold), and indicate as bifurcation points the existence of nearby $\epsilon > 0$ branches which may subsequently be followed. For symmetric problems with one-dimensional orbits of solutions, this procedure thus provides a reasonable means for computing imperfect bifurcation diagrams, at an additional (but not overwhelming) computational cost of numerically computing the entire orbit $\mathcal{S}_{triv}(\mathbf{z}_0)$.

Further difficulties arise, however, if one tries to perturb from the torus $\mathcal{S}_{nontriv}(\mathbf{z}_0)$, since one then must search within the two-dimensional orbit for ϵ-bifurcation points, and most existing parameter continuation algorithms compute only one-dimensional branches of equilibria. Li and Maddocks [10] propose one algorithm for this "torus search", involving successive breaking of two different symmetries, so that at each step only one-dimensional branches of equilibria exist. However, this algorithm is significantly harder to implement effectively than the perturbation from $\mathcal{S}_{triv}(\mathbf{z}_0)$ described above.

The goal of the current article is to perform a perturbation calculation by which the locations (θ, β) of the ϵ-bifurcation points from either $\mathcal{S}_{triv}(\mathbf{z}_0)$ or $\mathcal{S}_{nontriv}(\mathbf{z}_0)$ may be determined *a priori*, from which we derive the following benefits:

(1) The ability to choose starting points on $\mathcal{S}_{triv}(\mathbf{z}_0)$ or $\mathcal{S}_{nontriv}(\mathbf{z}_0)$ from which immediate continuation to $\epsilon > 0$ branches is possible, thereby removing the computational costs of searching the circle or torus for ϵ-bifurcation points.

(2) To verify the observation that the typical case is that two (respectively four) $\epsilon > 0$ branches bifurcate from the circle (respectively the torus) of perfect ring equilibria, and further provide criteria for identifying "non-generic" perturbations $\hat{u}_i$ for which more than this number of bifurcating branches can exist.[‡]

[‡]The generic expectations arise because the problem has a variational structure so that some version of Morse

5 Perturbation expansion

For $\mathbf{z} = (\mathbf{r}, \mathbf{q}, \mathbf{n}, \boldsymbol{\mu})$, the Hamiltonian BVP (3,7) takes the general form:

$$\mathbf{z}' = \mathbf{J}\frac{\partial H}{\partial \mathbf{z}}(\mathbf{z}, \epsilon), \quad \mathbf{A}\mathbf{z}(0) + \mathbf{B}\mathbf{z}(1) = \mathbf{g}(\alpha). \tag{11}$$

for $\mathbf{z}, \mathbf{f}, \mathbf{g} \in \mathbb{R}^{2n}$, and $\mathbf{A}, \mathbf{B} \in \mathbb{R}^{2n\times 2n}$ certain constant matrices. Here, $\mathbf{J} \in \mathbb{R}^{2n\times 2n}$ is the standard symplectic matrix:

$$\mathbf{J} = \begin{bmatrix} \mathbf{0}_n & \mathbf{I}_n \\ -\mathbf{I}_n & \mathbf{0}_n \end{bmatrix},$$

with $\mathbf{I}_n$ the n-by-n identity matrix and $\mathbf{0}_n$ the n-by-n matrix of zeroes. The functions $\mathbf{z}_{\theta\beta}$ are all solutions to (11) when $\epsilon = 0$, and we seek values (θ, β) for which a nearby solution exists for $\epsilon > 0$:

$$\mathbf{z} = \mathbf{z}_{\theta\beta} + \epsilon\bar{\mathbf{z}} + O(\epsilon^2). \tag{12}$$

In order to find such (θ, β), we insert the perturbation expansion (12) into (11) and collect terms in powers of ϵ. As is typical, the ϵ^0 terms yield the known equilibrium equations (11) for $\mathbf{z} = \mathbf{z}_{\theta\beta}$ and $\epsilon = 0$. The ϵ^1 terms are as follows:

$$\bar{\mathbf{z}}' = \mathbf{J}\frac{\partial^2 H}{\partial \mathbf{z}^2}(\mathbf{z}_{\theta\beta}, 0)\bar{\mathbf{z}} + \mathbf{J}\frac{\partial^2 H}{\partial \mathbf{z}\partial\epsilon}(\mathbf{z}_{\theta\beta}, 0), \quad \mathbf{A}\bar{\mathbf{z}}(0) + \mathbf{B}\bar{\mathbf{z}}(1) = \mathbf{0}. \tag{13}$$

We multiply the differential equation in (13) by $\mathbf{J}$ to reach the self-adjoint non-homogeneous linear system[§]

$$\mathcal{L}\bar{\mathbf{z}} = -\frac{\partial^2 H}{\partial \mathbf{z}\partial\epsilon}(\mathbf{z}_{\theta\beta}, 0), \quad \mathbf{A}\bar{\mathbf{z}}(0) + \mathbf{B}\bar{\mathbf{z}}(1) = \mathbf{0}, \tag{14}$$

where the linear operator $\mathcal{L}$ is defined by:

$$\mathcal{L}\mathbf{y} \equiv \mathbf{J}\mathbf{y}' + \frac{\partial^2 H}{\partial \mathbf{z}^2}(\mathbf{z}_{\theta\beta}, 0)\mathbf{y}. \tag{15}$$

Using the self-adjoint case of the standard alternative theorem (see, e.g. [13], Ch. 3.4), (14) has a solution $\bar{\mathbf{z}}$ if and only if the right-hand side $-\frac{\partial^2 H}{\partial \mathbf{z}\partial\epsilon}(\mathbf{z}_{\theta\beta}, 0)$ is L^2-orthogonal to the nullspace of $\mathcal{L}$, i.e. to all $\mathbf{y}$ satisfying:

$$\mathcal{L}\mathbf{y} = \mathbf{0}, \quad \mathbf{A}\mathbf{y}(0) + \mathbf{B}\mathbf{y}(1) = \mathbf{0}. \tag{16}$$

---

theory [12] could in principle be applied. According to Morse theory, under appropriate genericity assumptions, a circle of critical points will split to two critical points, a maximum and a minimum of the perturbed potential on the unperturbed circle. Similarly, the topology of the torus forces four critical points.

[§]Self-adjointness does not follow for arbitrary boundary conditions as in (11), but does hold for the particular boundary conditions in (7).

We may use the continuous symmetries present in the ideal problem to directly generate solutions to (16), namely $\partial\mathbf{z}_{\theta\beta}/\partial\theta$ and $\partial\mathbf{z}_{\theta\beta}/\partial\beta$ (this is easily verified by inserting $\mathbf{z}_{\theta\beta}$ in (11) and differentiating with respect to θ and β).

Thus, in order for an $\epsilon > 0$ branch to begin at $\mathbf{z}_{\theta\beta}$, we must have:

$$\int_0^1 \left(\frac{\partial\mathbf{z}_{\theta\beta}}{\partial\theta}\right)^T \frac{\partial^2 H}{\partial\mathbf{z}\partial\epsilon}(\mathbf{z}_{\theta\beta}, 0)\, ds = 0, \tag{17}$$

and

$$\int_0^1 \left(\frac{\partial\mathbf{z}_{\theta\beta}}{\partial\beta}\right)^T \frac{\partial^2 H}{\partial\mathbf{z}\partial\epsilon}(\mathbf{z}_{\theta\beta}, 0)\, ds = 0. \tag{18}$$

Note that we have not yet ruled out the possibility that $\mathcal{L}$ has other nullvectors independent of $\partial\mathbf{z}_{\theta\beta}/\partial\theta$ and $\partial\mathbf{z}_{\theta\beta}/\partial\beta$ (for example, an additional null-vector exists at folds on the nontrivial branches, i.e. where α changes direction). Thus, for now we can only say that (17) and (18) are necessary conditions for an $\epsilon > 0$ branch to begin at $\mathbf{z}_{\theta\beta}$.

6 Results

For the particular Hamiltonian system (3),

$$\mathbf{J}\frac{\partial H}{\partial\mathbf{z}} = \begin{bmatrix} \mathbf{d}_3(\mathbf{q}) \\ \frac{1}{2}\sum_{i=1}^3 \left(\epsilon\hat{u}_i\mathbf{B}_i\mathbf{q} + \frac{\boldsymbol{\mu}^T\mathbf{B}_i\mathbf{q}}{2K_i}\mathbf{B}_i\mathbf{q}\right) \\ \mathbf{0} \\ \frac{1}{2}\sum_{i=1}^3 \left(\epsilon\hat{u}_i\mathbf{B}_i\boldsymbol{\mu} + \frac{\boldsymbol{\mu}^T\mathbf{B}_i\mathbf{q}}{2K_i}\mathbf{B}_i\boldsymbol{\mu}\right) - \frac{\partial\mathbf{d}_3}{\partial\mathbf{q}}^T\mathbf{n} \end{bmatrix},$$

so that:

$$\mathbf{J}\frac{\partial^2 H}{\partial\mathbf{z}\partial\epsilon} = \begin{bmatrix} \mathbf{0} \\ \frac{1}{2}\sum_{i=1}^3 \hat{u}_i\mathbf{B}_i\mathbf{q} \\ \mathbf{0} \\ \frac{1}{2}\sum_{i=1}^3 \hat{u}_i\mathbf{B}_i\boldsymbol{\mu} \end{bmatrix}.$$

Therefore,

$$\frac{\partial^2 H}{\partial\mathbf{z}\partial\epsilon} = -\mathbf{J}\begin{bmatrix} \mathbf{0} \\ \frac{1}{2}\sum_{i=1}^3 \hat{u}_i\mathbf{B}_i\mathbf{q} \\ \mathbf{0} \\ \frac{1}{2}\sum_{i=1}^3 \hat{u}_i\mathbf{B}_i\boldsymbol{\mu} \end{bmatrix} = \begin{bmatrix} \mathbf{0} \\ -\frac{1}{2}\sum_{i=1}^3 \hat{u}_i\mathbf{B}_i\boldsymbol{\mu} \\ \mathbf{0} \\ \frac{1}{2}\sum_{i=1}^3 \hat{u}_i\mathbf{B}_i\mathbf{q} \end{bmatrix}.$$

Thus, condition (17) can be rewritten as:

$$\int_0^1 \sum_{i=1}^3 \hat{u}_i(s)\left[\frac{\partial\boldsymbol{\mu}_{\theta\beta}(s)}{\partial\theta}^T\mathbf{B}_i\mathbf{q}_{\theta\beta}(s) - \frac{\partial\mathbf{q}_{\theta\beta}(s)}{\partial\theta}^T\mathbf{B}_i\boldsymbol{\mu}_{\theta\beta}(s)\right] ds = 0, \tag{19}$$

and condition (18) can be rewritten as:

$$\int_0^1 \sum_{i=1}^{3} \hat{u}_i(s) \left[\frac{\partial \boldsymbol{\mu}_{\theta\beta}(s)}{\partial \beta}^T \mathbf{B}_i \mathbf{q}_{\theta\beta}(s) - \frac{\partial \mathbf{q}_{\theta\beta}(s)}{\partial \beta}^T \mathbf{B}_i \boldsymbol{\mu}_{\theta\beta}(s) \right] \, ds = 0, \tag{20}$$

The derivatives of $\boldsymbol{\mu}_{\theta\beta}$ and of $\mathbf{q}_{\theta\beta}$ can be computed from (9). After significant simplification (done using Mathematica), condition (19) simplifies to:

$$f_1(\theta, \beta) \equiv I_1(\beta) \cos\theta + I_2(\beta) \sin\theta = 0, \tag{21}$$

and (20) simplifies to:

$$\frac{m_3}{K_3}(1-\gamma)\left[I_1(\beta)\cos\theta + I_2(\beta)\sin\theta\right] - \left[I_3(\beta)\cos\theta + I_4(\beta)\sin\theta\right] = 0,$$

which, using (21), can immediately be further simplified to:

$$f_2(\theta, \beta) \equiv I_3(\beta) \cos\theta + I_4(\beta) \sin\theta = 0. \tag{22}$$

The central quantities appearing in the bifurcation conditions (21) and (22) are the integrals:

$$\begin{aligned}
I_1(\beta) &= \int_0^1 \left[-\hat{u}_1(s) m_2(s+\beta) + \hat{u}_2(s) m_1(s+\beta)\right] \, ds, \\
I_2(\beta) &= \int_0^1 \left[\hat{u}_1(s) m_1(s+\beta) + \hat{u}_2(s) m_2(s+\beta)\right] \, ds, \\
I_3(\beta) &= \int_0^1 \left[-\hat{u}_1(s) \mathbf{n}_0^T \mathbf{d}_2(\mathbf{q}_0(s+\beta)) + \hat{u}_2(s) \mathbf{n}_0^T \mathbf{d}_1(\mathbf{q}_0(s+\beta))\right] \, ds, \\
I_4(\beta) &= \int_0^1 \left[\hat{u}_1(s) \mathbf{n}_0^T \mathbf{d}_1(\mathbf{q}_0(s+\beta)) + \hat{u}_2(s) \mathbf{n}_0^T \mathbf{d}_2(\mathbf{q}_0(s+\beta))\right] \, ds.
\end{aligned} \tag{23}$$

Here, m_i are the moments of the reference configuration $\mathbf{z}_0$, defined by:

$$m_i(s) \equiv \frac{\boldsymbol{\mu}_0^T(s) \mathbf{B}_i \mathbf{q}_0(s)}{2}, \tag{24}$$

and as is well known (see e.g. [4, 10]), $m_3(s)$ is in fact independent of s for $\mathbf{z}_0$ a perfect ring equilibrium. In the expressions (23) and (24), the following rule must be used:

$$\begin{aligned}
\mathbf{q}_0(t) &\equiv \mathbf{M}_4(0,t)\mathbf{q}_0(t-1), \quad \text{for } t \geq 1, \\
\boldsymbol{\mu}_0(t) &\equiv \mathbf{M}_4(0,t)\boldsymbol{\mu}_0(t-1), \quad \text{for } t \geq 1.
\end{aligned}$$

Note that the intrinsic twist $\hat{u}_3(s)$ plays no role in these bifurcation conditions.

7 Analysis of results on trivial branch

If $\mathbf{z}_0$ is on a trivial branch, recall from Sec. 3 that the β dependence of the orbit collapses, so the necessary condition for an $\epsilon > 0$ branch to begin at $\mathbf{z}_{\theta 0}$ is simply (17), or its simplification (21), at $\beta = 0$:

$$f_1(\theta, 0) = I_1(0)\cos\theta + I_2(0)\sin\theta = 0. \tag{25}$$

Further, in this case we have shown (by directly solving the boundary value problem (16) in Mathematica) that, as long as $\mathbf{z}_0$ is not an α-bifurcation point, the *only* nullvectors of $\mathcal{L}$ are multiples of $\partial\mathbf{z}_{\theta 0}/\partial\theta$, so that condition (25) is in fact *sufficient* for bifurcation to imperfect solutions (at least within the usual level of rigor of perturbation expansions).

Using Eqs. (24) and (8), we find explicit expressions for the moments (m_1, m_2) on the trivial branch:

$$m_1(s) = 2K_1 N\pi\cos(\alpha s), \quad m_2(s) = -2K_1 N\pi\sin(\alpha s),$$

from which we derive explicit expressions for $I_1(0)$ and $I_2(0)$:

$$\begin{aligned} I_1(0) &= 2K_1 N\pi \int_0^1 \left[\hat{u}_1(s)\sin(\alpha s) + \hat{u}_2(s)\cos(\alpha s)\right]\, ds, \\ I_2(0) &= 2K_1 N\pi \int_0^1 \left[\hat{u}_1(s)\cos(\alpha s) - \hat{u}_2(s)\sin(\alpha s)\right]\, ds. \end{aligned} \tag{26}$$

Eq. (25) has the following solutions:

$$\theta = \begin{cases} \arctan(-I_1(0)/I_2(0)), \ \ \arctan(-I_1(0)/I_2(0)) + \pi, & \text{if } \ I_2(0) \neq 0, \\ \pi/2, \ \ 3\pi/2, & \text{if } \ I_2(0) = 0, I_1(0) \neq 0, \\ \text{any value between 0 and } 2\pi, & \text{if } \ I_2(0) = I_1(0) = 0. \end{cases} \tag{27}$$

Thus, exactly two branches will bifurcate from $\mathcal{S}_{triv}(\mathbf{z}_0)$ except in the special case

$$I_1(0) = I_2(0) = 0. \tag{28}$$

In this special degenerate case, a higher-order perturbation expansion is necessary in order to determine the behavior of the symmetry-breaking.

8 Analysis of results on nontrivial branch

If $\mathbf{z}_0$ is on a nontrivial branch, then we have seen that a necessary condition for an $\epsilon > 0$ branch to begin at $\mathbf{z}_{\theta\beta}$ is that $f_1(\theta, \beta) = f_2(\theta, \beta) = 0$.

Lemma 1: The solutions to $f_1(\theta, \beta) = f_2(\theta, \beta) = 0$ are:
(1) Two solutions (θ, β) and $(\theta + \pi, \beta)$ for each $0 \leq \beta < \frac{1}{M+N}$ with

$$I_1(\beta)I_4(\beta) - I_2(\beta)I_3(\beta) = 0, \quad I_i(\beta) \neq 0 \ \text{ for some } \ i.$$

(2) A line of solutions $\{(\theta, \beta) : 0 \leq \theta < 2\pi\}$ for each $0 \leq \beta < \frac{1}{M+N}$ with

$$I_1(\beta) = I_2(\beta) = I_3(\beta) = I_4(\beta) = 0.$$

Proof: It is clear that if $I_1(\beta) = I_2(\beta) = I_3(\beta) = I_4(\beta) = 0$, then $f_1(\theta) = f_2(\theta) = 0$ for all θ, so we henceforth assume $I_j(\beta) \neq 0$ for some j. Write (21) and (22) as a linear system:

$$\mathbf{M}(\beta) \begin{bmatrix} \cos\theta \\ \sin\theta \end{bmatrix} \equiv \begin{bmatrix} I_1(\beta) & I_2(\beta) \\ I_3(\beta) & I_4(\beta) \end{bmatrix} \begin{bmatrix} \cos\theta \\ \sin\theta \end{bmatrix} = \begin{bmatrix} 0 \\ 0 \end{bmatrix}. \tag{29}$$

Since $\cos\theta$ and $\sin\theta$ can not simultaneously vanish, (29) only has a solution if the matrix $\mathbf{M}(\beta)$ is singular, i.e. if $I_1(\beta)I_4(\beta) - I_2(\beta)I_3(\beta) = 0$. Further, since at least one of the I_j is nonzero, $\mathbf{M}(\beta)$ must be rank-one, which means there are exactly two unit null-vectors for $\mathbf{M}$, call them $\pm\mathbf{v}$. The Lemma then follows from the one-to-one correspondence between unit vectors $\mathbf{w}$ and values of $\theta \in [0, 2\pi)$ for which

$$\begin{bmatrix} \cos\theta \\ \sin\theta \end{bmatrix} = \mathbf{w}.$$

□

From Lemma 1, we see that the orbit of a nontrivial perfect ring equilibrium will contain $2k$ ϵ-bifurcation points, where k is the number of roots of $I_1 I_4 - I_2 I_3$ in the interval $0 \leq \beta < \frac{1}{M+N}$, as long as some I_j is nonzero at each of these roots. If $I_1 = I_2 = I_3 = I_4 = 0$ for some β, then a higher-order perturbation expansion is required to determine the behavior under symmetry-breaking.

Lemma 2: $I_1(\beta)I_4(\beta) - I_2(\beta)I_3(\beta) = 0$ for at least two values $\beta \in [0, \frac{1}{M+N})$.

Proof:

The balance of moments within the rod can be expressed as (see, e.g. [1], Ch. VIII)

$$\frac{d}{ds}\left(m_1\mathbf{d}_1 + m_2\mathbf{d}_2 + m_3\mathbf{d}_3\right) + \mathbf{d}_3 \times \mathbf{n} = \mathbf{0},$$

which is implied by a reformulation of the $\boldsymbol{\mu}'$ equation in (3). Expanding this equation using (1) gives:

$$m_1' = m_2 u_3 - m_3 u_2 + n_2, \qquad m_2' = m_3 u_1 - m_1 u_3 - n_1,$$

where $n_i \equiv \mathbf{n}^T\mathbf{d}_i$. If we further use the fact that $m_i = K_i u_i$ on a perfect equilibrium (cf. (2)) and that $K_1 = K_2$, we find:

$$m_1' = u_3\left(1 - \frac{K_3}{K_1}\right) m_2 + n_2, \qquad m_2' = -u_3\left(1 - \frac{K_3}{K_1}\right) m_1 - n_1.$$

From these equations, and the fact that u_3 is independent of s for a perfect equilibrium, we find that

$$\frac{dI_1}{d\beta} = u_3 \left(1 - \frac{K_3}{K_1}\right) I_2 + I_4, \qquad \frac{dI_2}{d\beta} = -u_3 \left(1 - \frac{K_3}{K_1}\right) I_1 - I_3,$$

from which:

$$\frac{d}{d\beta}(I_1^2 + I_2^2) = I_1 \frac{dI_1}{d\beta} + I_2 \frac{dI_2}{d\beta} = I_1 I_4 - I_2 I_3. \tag{30}$$

Now, the symmetry arguments used in Sec. 3 to show that $\mathbf{z}_{\Delta\theta,1/(M+N)} = \mathbf{z}_0$ can also be used to show that:

$$\begin{aligned} m_1\left(s + \frac{1}{M+N}\right) &= \cos(\Delta\theta) m_1(s) - \sin(\Delta\theta) m_2(s), \\ m_2\left(s + \frac{1}{M+N}\right) &= \sin(\Delta\theta) m_1(s) + \cos(\Delta\theta) m_2(s). \end{aligned}$$

From these expressions, it is easily verified that

$$\left[I_1\left(\frac{1}{M+N}\right)\right]^2 + \left[I_2\left(\frac{1}{M+N}\right)\right]^2 = [I_1(0)]^2 + [I_2(0)]^2 .$$

Hence, the function $[I_1(\beta)]^2 + [I_2(\beta)]^2$ is periodic of period $\frac{1}{M+N}$ and therefore must have at least two critical points $\beta \in [0, \frac{1}{M+N})$. Using (30), this implies that $I_1 I_4 - I_2 I_3$ has at least two zeroes in this same interval.$\square$

With Lemmas 1 and 2, we see that there are always at least four solutions (θ, β) to $f_1 = f_2 = 0$, and hence at least four ϵ-bifurcation points on the orbit of a nontrivial ring equilibrium.

9 Examples and Discussion

For a given perturbation $(\hat{u}_1(s), \hat{u}_2(s))$, we may use the conditions (21) and (22) to determine the manner of the symmetry-breaking of the perfect bifurcation diagram in Fig. 3. The simplest type of symmetry-breaking, as outlined in [10], is depicted in Fig. 6, in which each perfect trivial branch (on which the orbits are circles) yields two images in the imperfect diagram, while each perfect nontrivial branch (on which the orbits are tori) yields four. In this Figure, we have added a second plot in which a third axis $m_1(0)$ is added and a small rotation is made about $m_3(0)$. In this way, we highlight the splitting between the perturbed branches, since $m_1(0)$ is a quantity that changes significantly along the orbit of solutions to the perfect problem. In fact, for the perfect problem, at each $(m_3(0), E)$, $m_1(0)$ sweeps over an entire interval of possible values $-M \leq m_1(0) \leq M$ as the orbit (for fixed α) is traversed, so Fig. 3 could be regarded as the view down the $m_1(0)$ axis of the three-dimensional cylindrical surface in $(m_3(0), E, m_1(0))$ space. With the perturbation analysis presented here, it may now be concluded that this type of symmetry-breaking results precisely when the following conditions hold:

Condition 1: There is no perfect ring equilibrium on a trivial branch (i.e. value of α) for which $I_1(0) = I_2(0) = 0$ (cf. (26)).
Condition 2: There is no perfect ring equilibrium on a nontrivial branch for which $I_1(\beta) = I_2(\beta) = I_3(\beta) = I_4(\beta) = 0$ for some value of β.
Condition 3: For each perfect ring equilibrium on $(M, N, \pm)^{nontriv}$, $I_4(\beta)I_1(\beta) - I_2(\beta)I_3(\beta) = 0$ has only two roots $\beta \in [0, \frac{1}{M+N})$.

Further, when all three conditions are satisfied, the entire imperfect diagram may be computed by the following algorithm:

- Choose a single perfect ring equilibrium $\mathbf{z}_0$ on each $(M, N, \pm)^{triv}$ of the perfect diagram.
- With ϵ the continuation parameter, compute the two branches of equilibria that bifurcate from the circle $\mathcal{S}_{triv}(\mathbf{z}_0)$, for $0 < \epsilon \leq 1$.
- Once $\epsilon = 1$, make the twist angle α the continuation parameter, and follow the branch of (imperfect) ring equilibria until this branch closes up on itself.

This was the procedure prescribed in [10], and applied in [11] for intrinsic shapes $(\hat{u}_1, \hat{u}_2)$ derived from the base-pair-dependent structure of eleven DNA molecules. We have now numerically verified that Conditions 1–3 do in fact hold (at least for the lowest-energy branches $(1, 1, +)^{triv}$, $(1, 1, +)^{nontriv}$, and $(1, 1, -)^{triv}$) for these eleven perturbations.

When this algorithm was applied in [10] and [11], the second step (computing the branches bifurcating from the orbit) required first numerically generating the entire orbit, as described in Sec. 4. Armed with the current analysis, however, it is possible to choose an initial solution $\mathbf{z}_{\theta 0}$ close to a desired ϵ-bifurcation point and thus locate the bifurcating branches in a small number of steps along the orbit. Better still is an algorithm which jumps directly onto the bifurcating branches, in which we choose a small positive initial value for ϵ, with initial $\mathbf{z}$ at the ϵ-bifurcation point. This latter algorithm works equally well for orbits of any dimension. Of course, the instability of parameter-continuation algorithms with starting points at bifurcation points is well known, so a better initial solution would be the first two terms in the perturbation expansion $\mathbf{z} = \mathbf{z}_{\theta\beta} + \epsilon\bar{\mathbf{z}}$, once an efficient computation for the first-order term $\bar{\mathbf{z}}$ is developed.

The failure of any of Conditions 1–3 can cause a significant change in the qualitative structure of the imperfect diagram. The failure of either Conditions 1 or 2 implies that a higher-order perturbation expansion is required to categorize the symmetry-breaking. Not surprisingly, a wide catalogue of behaviors can be found within this set of degenerate perturbations, as shown in Figs. 7 and 8 (a smaller portion of the diagram is shown than in previous figures in order to focus on the regions of unusual branch splitting).

In contrast to the failure of Conditions 1 or 2, the failure of Condition 3 implies the existence of $k > 2$ zeros of $I_4I_1 - I_2I_3$ (recall from Sec. 8 that $I_4I_1 - I_2I_3$ must have at least two zeros $\beta \in [0, \frac{1}{M+N})$). This in turn implies the existence of $2k > 4$ branches bifurcating from the torus $\mathcal{S}_{nontriv}(\mathbf{z}_0)$ (if $I_4I_1 - I_2I_3$ were identically zero on any interval, a higher-order perturbation would be required to determine the resulting behavior). In Fig. 9, we see an imperfect diagram for a perturbation for which Condition 3 fails, with $k = 4$ on two intervals on $(1, 1, +)^{nontriv}$. In addition, for this perturbation, Condition 1 nearly fails at $\alpha \approx 6$ on $(1, 1, \pm)^{triv}$, as reflected by the spikes on the perturbed trivial segments.

In the imperfect diagrams in Figs. 7—9, AUTO reported no α-bifurcation points, so that all branch intersections in the figures are artifacts of the two-dimensional plots. Nevertheless, it does appear that each of these imperfect problems is close to another imperfect problem with α-bifurcation points. Furthermore, these "approximate" α-bifurcation points appear to occur exactly at the locations where one of Conditions 1–3 fail: near the small oval at the bottom of Fig. 7, near the three small ovals in Fig. 8, and near the whorls in the center of Fig. 9.

Note that three of the four imperfect diagrams shown here (i.e. all those except for Fig. 8) have the same left-right symmetry as the perfect diagram. This is no doubt due to some other symmetry present in the special perturbations used as imperfections, but this type of symmetry is not a focus of the current paper.

In Fig. 9, the additional branches perturbing from $(1,1,+)^{nontriv}$ occur as whorls in branches connected to the perturbations of $(1,1,\pm)^{triv}$ or $(1,2,\pm)^{triv}$. However, it is conceivable that when Condition 3 fails, some of the $2k-4$ additional branches could occur as small *isolas*, i.e. loops that are completely disconnected from the components of the diagram arising from the perturbations of the trivial branches. In that case, a computational algorithm (such as the one described at the beginning of this Section) that only follows branches perturbing from the trivial branches would fail to compute the entire imperfect diagram. Thus, the perturbation expansion presented here provides a test for when it may be necessary to search for branches perturbing from nontrivial branches, and further provides the locations on the nontrivial branches where these isolas may arise.

It may fairly be said that the set of perturbations for which symmetry-breaking differs qualitatively from the simple case shown in Fig. 6 are an exceptional set; a random perturbation $\hat{u}_i(s)$ should satisfy Conditions 1–2 with probability one, and Condition 3 also appears to hold quite generally. Still, the ability to pinpoint particular perturbations which defy this "generic" case is crucial for understanding the structures of imperfect diagrams, because the exceptional perturbations are the seeds of behaviors that are robust (i.e. occur for an open set of perturbations) for larger values of the perturbation parameter. In other words, the range of perturbations exhibiting the qualitative features of Figs. 7–9 tends to expand as ϵ increases.

For example, Katritch and Vologodskii report (and corresponding continuum computations confirm) two low-energy stable nicked loops in Monte Carlo simulations of several DNA molecules with significant intrinsic curvature [8]. In the terminology of the current paper, the Katritch and Vologodskii model of a "stable nicked loop" is a stable ring equilibrium with $m_3(0) = 0$, so the existence of two low-energy stable nicked loops is at odds with the picture of generic diagram splitting in Fig. 6 (stability has not been a focus of this article, but recall from Sec. 4 that only one of the two lower-most branches in Fig. 6 is stable). Based on the analysis presented here, however, we can see that the existence of multiple stable nicked loops at *large* perturbations can be predicted from the behavior of the exceptional case of *infinitesimal* perturbation:

$$I_1(0) = I_2(0) = 0 \ \text{ for } \ N = 1, \ \alpha = 0,$$

or more explicitly:

$$\int_0^1 \hat{u}_1(s)ds = \int_0^1 \hat{u}_2(s)ds = 0 \tag{31}$$

($N = 1$, $\alpha = 0$ being the unique stable nicked DNA loop for the perfect problem). Indeed, Katritch and Vologodskii report finding two stable nicked loops most readily for S-shaped molecules, and such intrinsic shapes approximately satisfy (31).

We have restricted attention here to the BVP corresponding to the twisted ring, and to perturbations affecting the intrinsic shape $\hat{u}_i(s)$, but the methods presented are quite general. For example, even within the twisted ring example, there are other perturbations of interest, including the addition of anisotropy in the bending stiffness $K_2 \neq K_1$, and the allowance of non-uniform stiffnesses $K_i(s)$. To treat these different perturbations, one merely computes the appropriately revised right-hand side in (14) and thus derives appropriately modified solvability conditions analogous to (17) and (18).

Acknowledgments: RSM was supported by an NSF Postdoctoral Research Fellowship.

References

[1] S. S. Antman. *Nonlinear Problems of Elasticity.* Springer-Verlag, New York, 1995.

[2] W. Bauer, R. Lund, and J. White. Twist and writhe of a DNA loop containing intrinsic bends. *Proc. Natl. Acad. Sci. USA*, 90:833–837, 1993.

[3] A. Bolshoy, P. McNamara, R. E. Harrington, and E. N. Trifonov. Curved DNA without A-A: Experimental estimation of all 16 wedge angles. *Proc. Natl. Acad. Sci. USA*, 88:2312–2316, 1991.

[4] D. J. Dichmann, Y. W. Li, and J. H. Maddocks. Hamiltonian formulations and symmetries in rod mechanics. In J.P. Mesirov, K. Schulten, and D.W. Sumners, editors, *Mathematical Approaches to Biomolecular Structure and Dynamics*, volume 82, pages 71–113. Springer, New York, New York, 1996. IMA Volumes in Mathematics and its Applications.

[5] E. J. Doedel, H. B. Keller, and J. P. Kernévez. Numerical analysis and control of bifurcation problems, parts I and II. *Int. J. of Bif. and Chaos*, 3, 4:493–520, 745–772, 1991.

[6] G. Domokos. A group-theoretic approach to the geometry of elastic rings. *J. Nonlinear Sci.*, 5:453–478, 1995.

[7] J. D. Foley, A. van Dam, S. K. Feiner, and J. F. Hughes. *Computer Graphics: Principles and Practice.* Addison-Wesley, New York, 1996.

[8] V. Katritch and A. Vologodskii. The effect of intrinsic curvature on conformational properties of circular DNA. *Biophysical Journal*, 72:1070–1079, 1997.

[9] S. Kehrbaum and J. H. Maddocks. Elastic rods, rigid bodes, quaternions and the last quadrature. *Phil. Trans. R. Soc. Lond. A*, 355:2117–2136, 1997.

[10] Y. Li and J. H. Maddocks. On the computation of equilibria of elastic rods, Part I: Integrals, symmetry and a Hamiltonian formulation. *J. Comp. Phys.*, to appear.

[11] R. S. Manning, J. H. Maddocks, and J. D. Kahn. A continuum rod model of sequence-dependent DNA structure. *J. Chem. Phys.*, 105:5626–5646, 1996.

[12] J. Milnor. *Morse Theory.* Princeton University Press, Princeton, New Jersey, 1970.

[13] I. Stakgold. *Green's Functions and Boundary Value Problems.* John Wiley, New York, 1979.

[14] Y. Yang, I. Tobias, and W. Olson. Finite element analysis of DNA supercoiling. *J. Chem. Phys.*, 98:1673–1686, 1993.

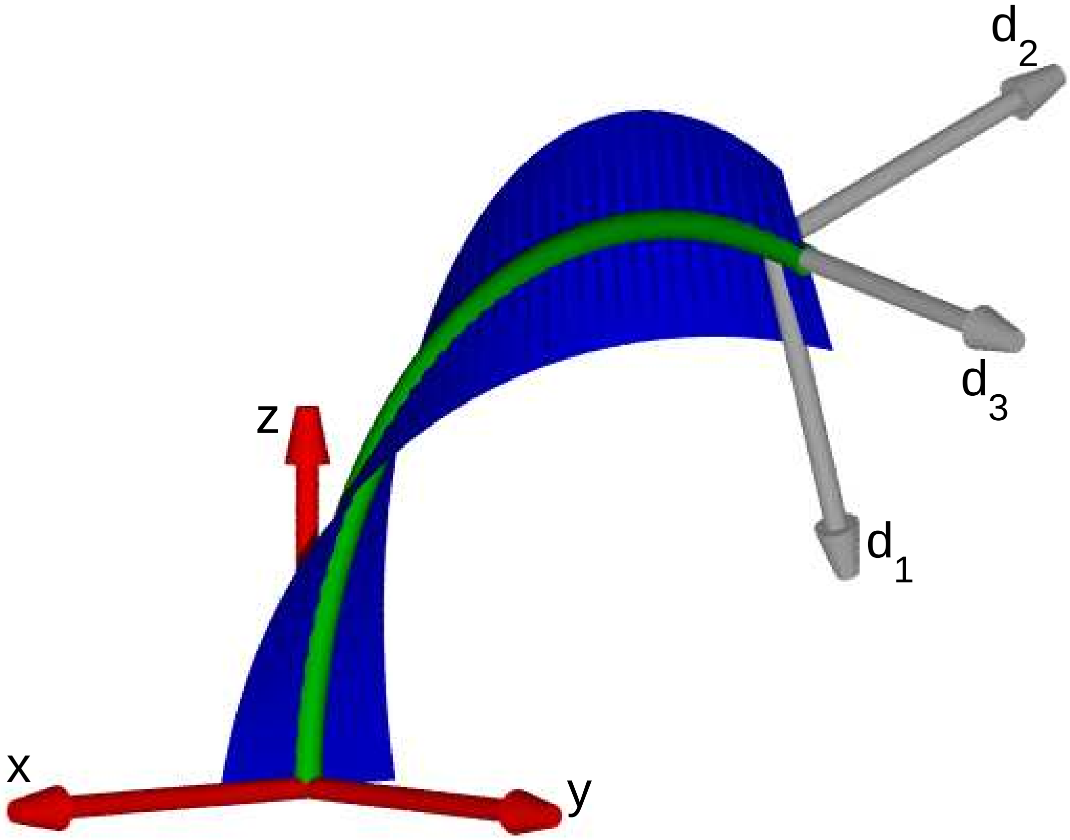

Figure 1: An elastica: the centerline $\mathbf{r}(s)$ is represented by a tube, and the director $\mathbf{d}_1(s)$ by a ribbon.

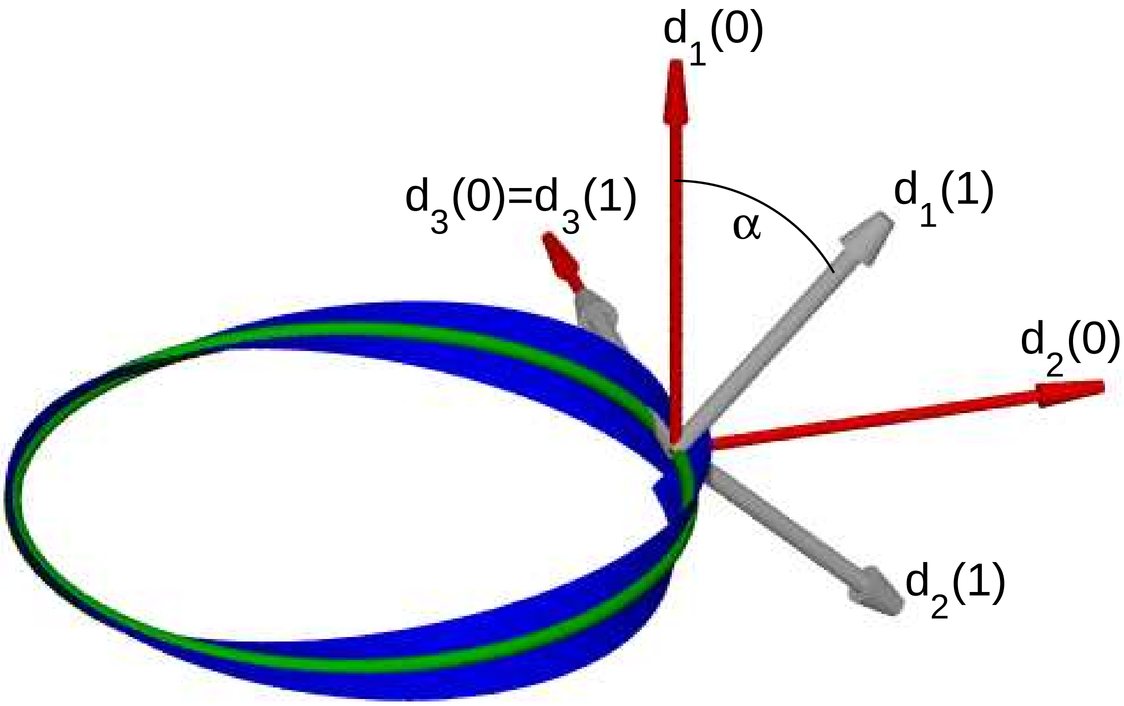

Figure 2: The twisted elastic ring: the centerline $\mathbf{r}(s)$ is constrained to form a loop, and a twist angle α is imposed between the directors $\mathbf{d}_1(0)$ and $\mathbf{d}_1(1)$.

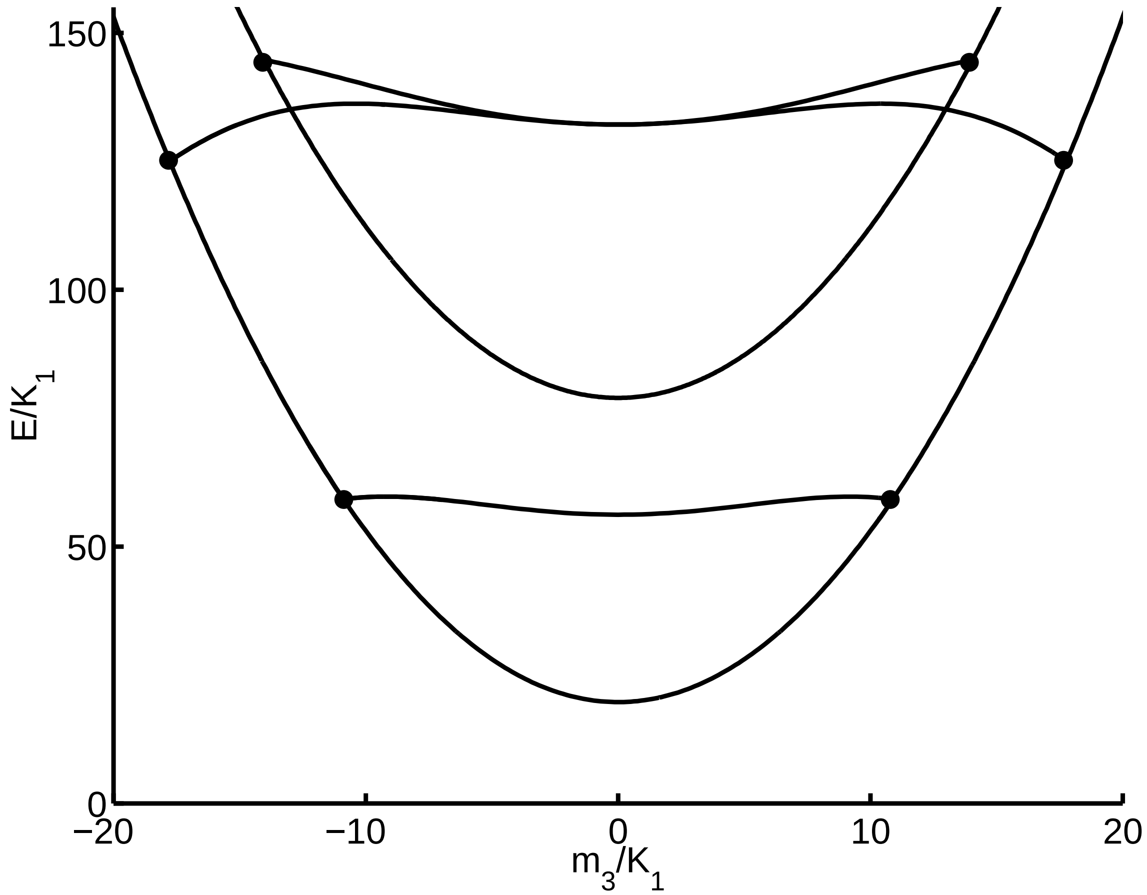

Figure 3: Lower portion of the bifurcation diagram for the perfect problem. As the twist parameter α is varied, the energy E and twist moment m_3 of the ring equilibria are plotted. The parabolic (*trivial*) branches correspond to planar equilibria with circular centerlines, and the remaining (*nontrivial*) branches correspond to nonplanar equilibria. Branch intersections (i.e., α-bifurcation points) are marked by dots; all other apparent branch intersections in the figure are artifacts of the two-dimensional projection used here.

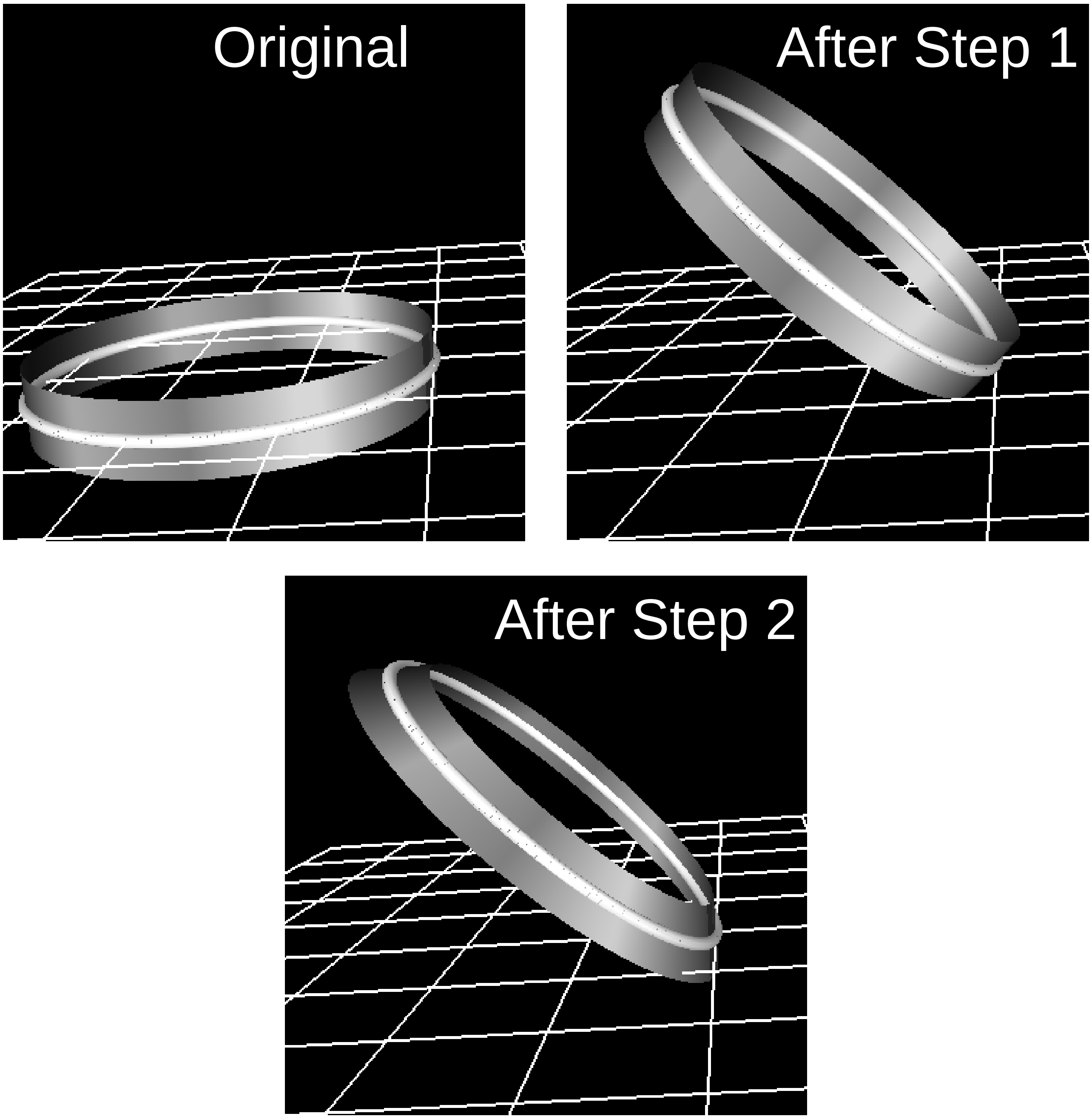

Figure 4: Transformation I: The original solution and its images after Steps 1 and 2, for $\theta = 45°$. The z axis lies on the grid, pointing away from the viewer.

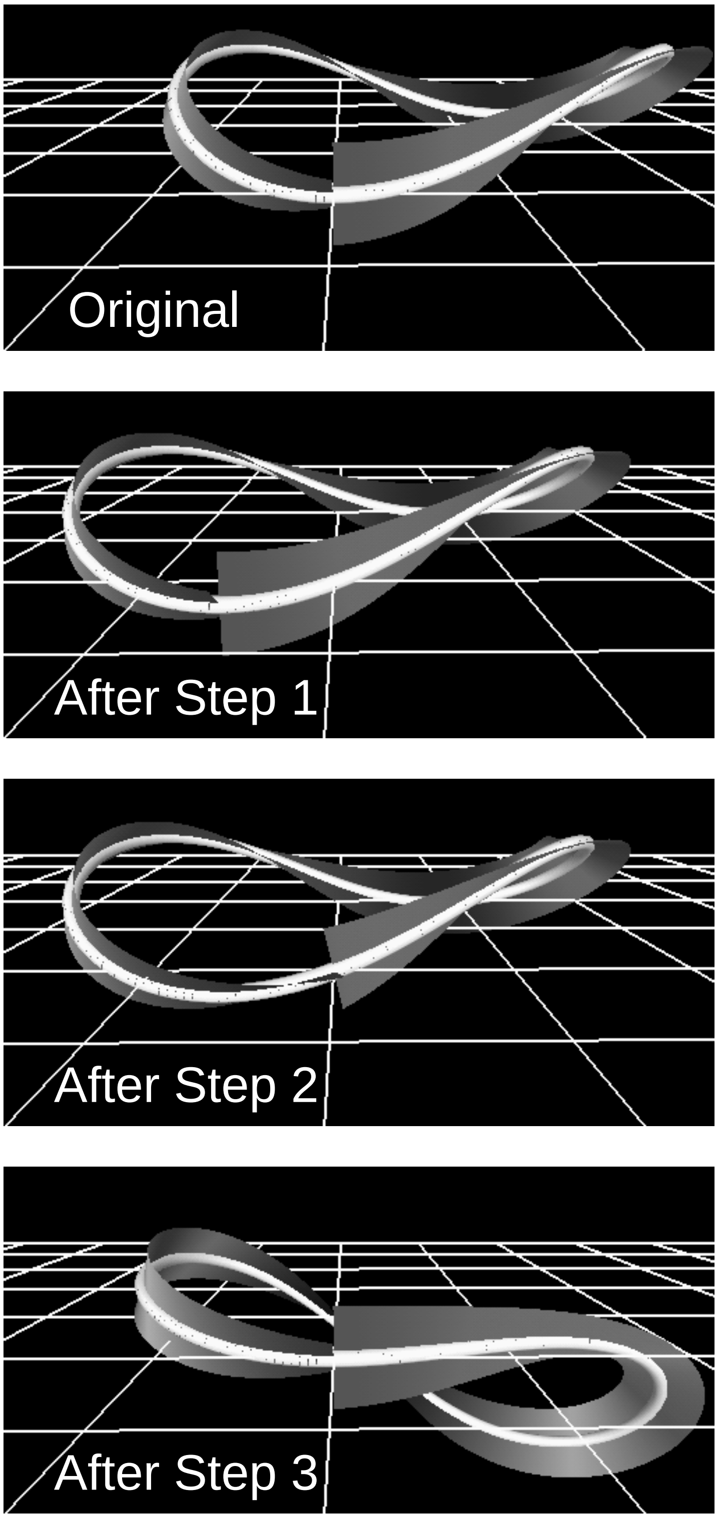

Figure 5: Transformation II: The original solution and its images after Steps 1 through 3, for $\beta \approx 0.06$. The z axis lies on the grid, pointing to the right.

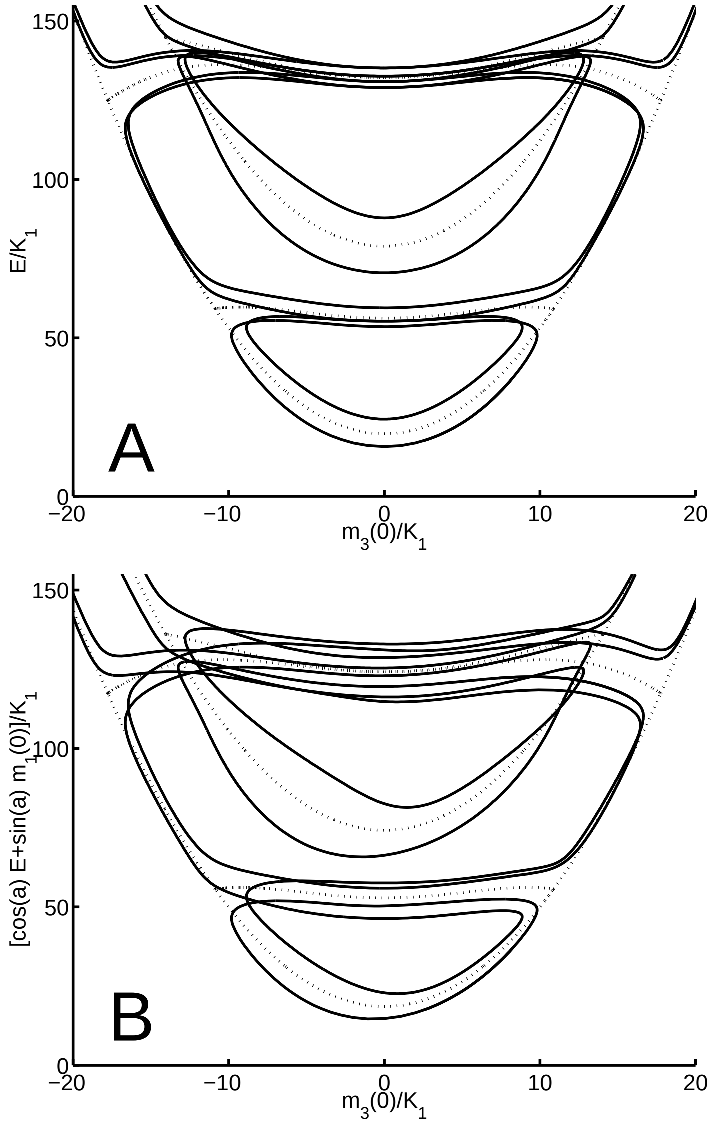

Figure 6: Lower portion of bifurcation diagram (solid line) for a "generic" perturbation ($\hat{u}_1(s) = 0, \hat{u}_2(s) = 1.5 \sin s$). The perfect bifurcation diagram from Fig. 3 is also plotted for comparison (dotted line). Plot A contains the plan view of E versus $m_3(0)$ used in Fig. 3, while in Plot B, a third axis $m_1(0)$ is added and a rotation with $a = 20°$ is made about the $m_3(0)$ axis to better show the branch splitting. Since solutions on the orbits of the perfect problem have different values of $m_1(0)$, a representative with $m_1(0) = 0$ has been selected for the dotted line in Plot B. The trivial branches from Fig. 3 have split into two branches, while the nontrivial branches have split into four. Note that the perfect branches $(1, 2, +)^{nontriv}$ and $(1, 2, -)^{nontriv}$ are quite close to each other in this projection (top center), and as a result their eight images under perturbation run together in Plot A. There are no α-bifurcation points in this imperfect diagram; all apparent branch intersections are artifacts of the chosen two-dimensional projections.

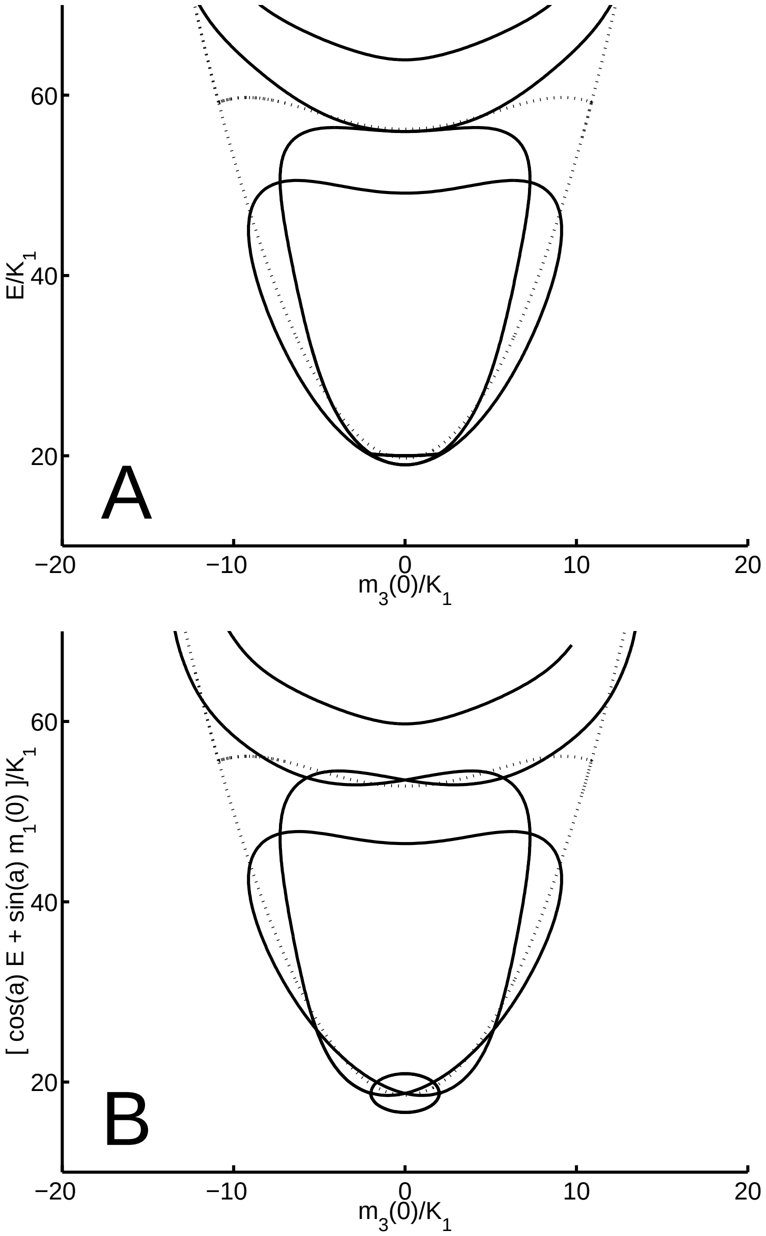

Figure 7: Lower portion of bifurcation diagram (solid line) for a perturbation ($\hat{u}_1 = 3\sin(1)s - 1.5\cos(s)$, $\hat{u}_2 = 0$) for which Condition 1 fails at $\alpha = 0$. Qualitatively, the diagram is similar to the lower portion of Fig. 6 with an additional branch at the bottom center. Axes are as in Fig. 6. The perfect diagram is shown with a dotted line.

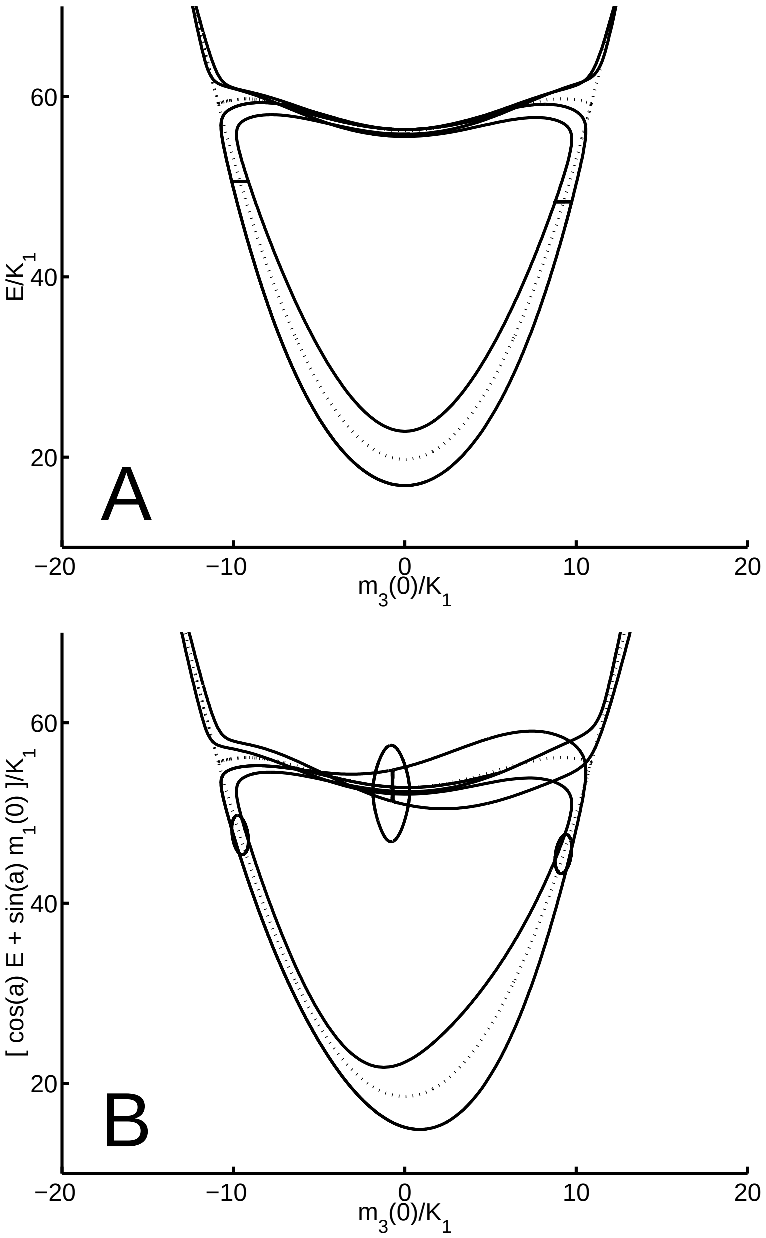

Figure 8: Lower portion of bifurcation diagram (solid line) for a perturbation ($\hat{u}_1(s) = -0.198 + 0.052s + 0.0013s^2$, $\hat{u}_2 = -0.437 - 0.024s + 0.0032s^2$) for which Condition 2 fails near the center of $(1,1,+)^{nontriv}$, and Condition 1 fails at a point on each of $(1,1,\pm)^{triv}$. Away from these three points, the diagram looks qualitatively like the lower portion of Fig. 6, but the behavior is more complicated near the three degeneracies, especially on the nontrivial branch. Axes are as in Fig. 6. The perfect diagram is shown with a dotted line.

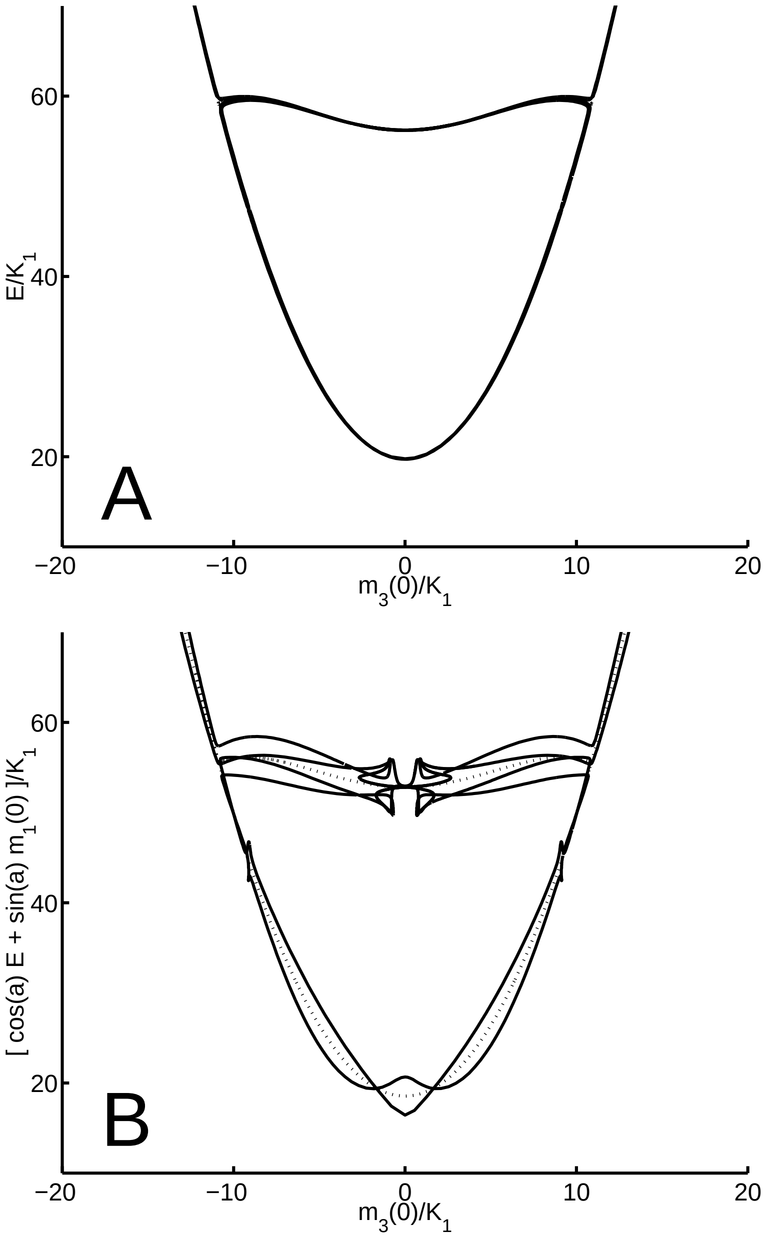

Figure 9: Lower portion of bifurcation diagram for a perturbation ($\hat{u}_1 = 0.2\sin(8\pi s) + 0.01s$, $\hat{u}_2 = 0$) for which two distinct segments of $(1,1,+)^{nontriv}$ splits into 8 branches (while the remainder splits into 4 branches as usual). In addition, Condition 1 nearly fails at $\alpha = 6$ for this perturbation, resulting in spikes on the perturbations of $(1,1,\pm)^{triv}$. Axes are as in Fig. 7. The perfect diagram is shown with a dotted line. In this case, the splitting of the imperfect diagram from the perfect diagram can not be easily detected in Plot A (but a larger value of ϵ would have obscured the qualitative understanding of the branch splitting shown in Plot B).